PREDICTION OF FRICTION DRAG IN PULSATING TURBULENT PIPE FLOW BY DEEP LEARNING FOR IMPROVEMENT OF GENERALIZATION CAPABILITY

Kazunori Matsubara, Akihiko Mitsuishi, Kaoru Iwamoto*, and Akira Murata
Department of Mechanical Systems Engineering
Tokyo University of Agriculture and Technology
2-24-16 Nakacho, Koganei, Tokyo 184-8588, Japan
* Corresponding author: iwamotok@cc.tuat.ac.jp

ABSTRACT

A new deep learning model was proposed to predict the spatiotemporal development of pulsating turbulent pipe flow. The model is referred to as the time delay NN-RNN model which is the combination of the previous long short-term memory (LSTM) encoder-decoder model and time delay neural network (TDNN). The flow field obtained by direct numerical simulation (DNS) was used to train the model. Being trained on data with different pulsation parameters from the test data, the time delay NN-RNN model predicts the skin friction coefficient more accurately than the previous model. Therefore, the generalizability of the model is improved.

BACKGROUND AND OBJECTIVES

Energy loss due to friction drag is a problem in the transportation of oil and natural gas through pipelines. One of the methods to reduce the friction drag is pulsating control. Considering that the turbulent vortices decrease/increase during acceleration/deceleration, the pulsation can yield drag reduction effect by carefully choosing the relevant parameters.

There have been many studies on drag reduction for pulsating turbulent flow. Manna and Vacca (2008) confirmed drag reduction rate up to 27% by large eddy simulation (LES) of pulsating turbulent pipe flow in the case where the amplitude of a sinusoidal wave of the streamwise pressure gradient to make the pulsation is very large. Lodahl et al. (1998) conducted experiments on pulsating turbulent pipe flow to investigate the variation of turbulence. The pulsating flow is regarded as a combination of oscillatory flow and current. It is found that the pulsating flow relaminarizes if the pulsating flow is oscillatory flow dominated and the oscillatory component of the flow is in the laminar flow regime.

In recent years, machine learning has been increasingly applied to the various problem of fluid mechanics (Brunton et al., 2020). Fan et al. (2021) proposed the CNN+LSTM module as an efficient alternative to the synthetic eddy method (SEM) which is time-consuming. The module could accurately predict turbulence statistics even after a long time and achieve over 15 times speedup compared with SEM. Giannopoulos and Aider (2020) predicted the full-field dynamics of backward-facing step (BFS) flow by focused time-delay neural network (FTDNN). Different upstream local visual sensors, based on the velocity fields measured by time-resolved particle image velocimetry (PIV), were tested as inputs for the NN system. The NN system could predict with satisfying precision the global dynamics of the flow. On the other hand, Yamaguchi et al. (2019) constructed a LSTM encoder-decoder model which could predict the time evolution of the flow field in pulsating turbulent pipe flow. The model successfully predicted a pulsatile flow when its pulsation parameters are the same as those of training data, but it failed when they are different.

The objective of this study is to improve the generalizability of the model. For that purpose, TDNN is introduced to the model of Yamaguchi et al. (2019). Then, the predictive performance of the model is evaluated when the training and predicting waves are different.

CALCULATION METHOD

DNS of Pulsating Turbulent Pipe Flow

In this study, the flow field of pulsating turbulent pipe flow was calculated by DNS. Governing equations are the continuity and Navier-Stokes equations. A highly energy-conservative second-order-accurate finite difference method for the cylindrical coordinate system (Fukagata and Kasagi, 2002) is employed for the spatial discretization scheme. The memory-saving third-order accurate Runge-Kutta method (Spalart et al., 1991) for the advection term and the Crank-Nicolson method for the diffusion term are employed for the time integration. The friction Reynolds number is set to $Re_\tau = u_\tau R/\nu = 180$, where u_τ is the friction velocity based on mean wall shear stress, R the pipe radius, and ν the kinematic viscosity. The computational domain is shown in Fig. 1. Here, r, θ, and z denote the radial, circumferential, and axial directions, respectively. The number of computational cells is (N_r, N_θ, N_z) = (96, 128, 256), and grid resolution is (Δr^+, $R^+\Delta\theta$, Δz^+) = (0.35−2.24, 8.83, 8.83). The radial grid width is small near the wall and large at the center of the pipe. Here, $()^+$ denotes the value normalized by u_τ and ν. The periodic boundary condition is used at θ and z directions, and the no-slip boundary condition is used at the pipe wall.

In the pulsating flow, the time change of spatially averaged streamwise pressure gradient is controlled to accelerate and decelerate the flow. In this study, the flow field is calculated by giving a sinusoidal pulsating wave as follows:

$$-\left\langle \frac{dp^*}{dz^*} \right\rangle = 2 + A^* \sin \frac{2\pi t^*}{T^*} \tag{1}$$

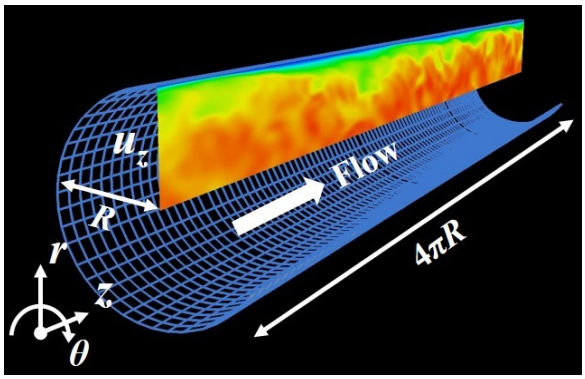

Figure 1. Computational domain.

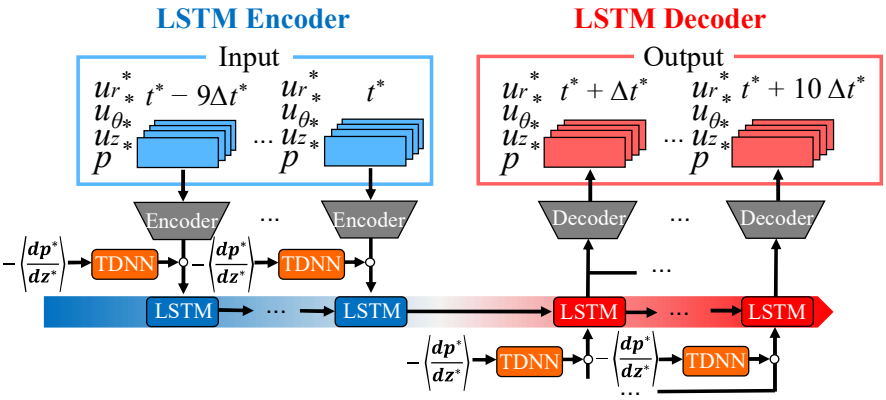

Figure 2. Time delay NN-RNN model.

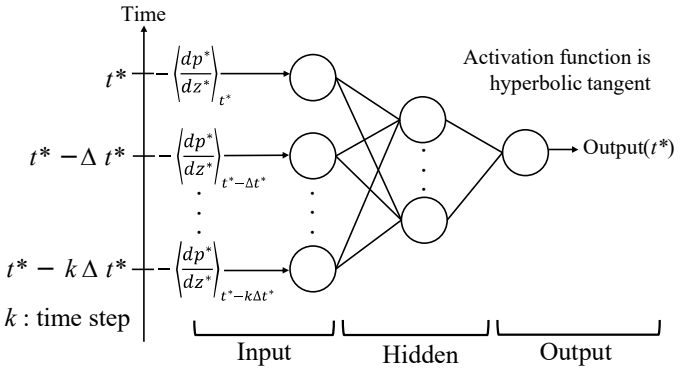

Figure 3. Structure of TDNN.

where A and T are amplitude and period, respectively. The angle brackets $< >$ denotes spatial averaged value, and $()^*$ denotes the value normalized by u_τ and R.

Deep Learning for DNS Data

The time delay NN-RNN model shown in Fig. 2 was constructed to predict the time evolution of flow fields: velocity and pressure (u_r^*, u_θ^*, u_z^*, p^*) in $r-z$ cross-section obtained by DNS. Here, the time interval of flow field Δt^* is set to 5×10^{-3}. The time delay NN-RNN model consists of the encoder, TDNN, LSTM, and decoder. Inputs to LSTM are flow fields convoluted by the encoder to 1/32 and features of spatially averaged streamwise pressure gradient extracted by TDNN. LSTM predicts the time evolution of the low dimensional flow field. Then, the output of LSTM is deconvoluted by the decoder to the original size.

In this study, TDNN was added to the model of Yamaguchi et al. (2019) to improve the generalizability of the model. TDNN is composed of three layers: input, hidden, and output layers as shown in Fig. 3. In addition to the pressure gradient at the current time, the pressure gradient up to k time steps before is also input into TDNN. Therefore, extracted features can be related to the time variation of the past pressure gradient. Several time steps k was tested and found $k = 2$ was the highest prediction accuracy. Thus, in this paper, we report the results of $k = 2$. The Adam algorithm is applied as the optimizer. The learning rate, the number of epochs, and the minibatch size are set to 0.001, 100, and 32, respectively. Here, the training data consist of 14,000 steps

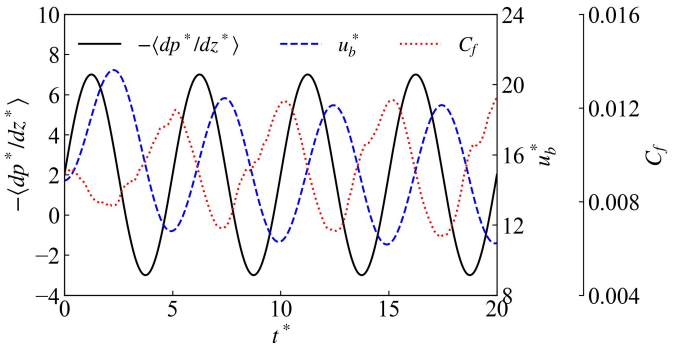

Figure 4. Time variation of spatially averaged pressure gradient, bulk velocity u_b^*, and skin friction coefficient C_f.

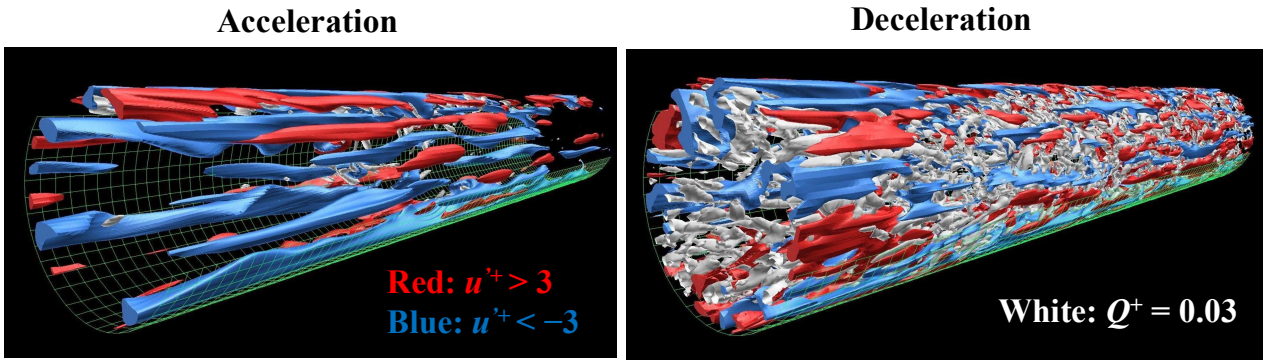

Figure 5. Visualization results of pulsating turbulent flow with high-speed streak (red), low-speed streak (blue), isosurface of the second invariant of velocity gradient tensor (white).

spanning $10 < t^* < 80$. The test data consist of 14,000 steps spanning $80 < t^* < 150$. Table 1 shows the amplitude and period of the sinusoidal pulsating wave for training data and test data. For each pulsating flow, one $r - z$ cross-section is used for training and prediction.

Table 1. Pulsation parameters for training and test data.

	(A^*, T^*)
Training data	(4, 5), (5, 4), (6, 5), (5, 6)
Test data	(5, 5)

RESULTS

Basic Characteristics of DNS Data

The flow fields with the sinusoidal pulsating wave of its amplitude $A^* = 5$ and period $T^* = 5$ were calculated by DNS. Figure 4 shows the time variation of spatially averaged pressure gradient, bulk velocity $u_b{}^*$, and skin friction coefficient C_f calculated by DNS. Here, the skin friction coefficient C_f is defined by the bulk velocity $u_b{}^*$ and the wall shear stress $\tau_w{}^*$, as shown in Eq. 2.

$$C_f = \frac{\tau_w{}^*}{\frac{1}{2}u_b{}^{*2}} \tag{2}$$

The phase of the bulk velocity delays by $\pi/2$ than the spatially averaged pressure gradient. The skin friction coefficient decreases in acceleration, and vice versa. Thus, the pulsating turbulent pipe flow is the unsteady turbulent flow, in which bulk velocity and skin friction coefficient temporally change.

Figure 5 shows visualization results of the high-speed and low-speed streaks, and vortex defined by the second invariant of velocity gradient tensor during acceleration and deceleration. It can be seen from the figure that the number of vortices decreases during acceleration and increases during deceleration. Comparing Figs. 4 and 5, it is found that the friction drag reduces by decreasing vortices during acceleration, and increases by increasing vortices during deceleration.

Figure 6 shows the radial profiles of the phase-averaged streamwise velocity, RMS value of phase-averaged streamwise velocity fluctuations, and Reynolds shear stress respectively. The red and blue line indicate acceleration and deceleration. Here, each line is mean value of the phase average in each interval shown in the legend of the figure. The phase for $0 < t^*/T^* < 1/6$, $1/6 < t^*/T^* < 1/3$, and $1/3 < t^*/T^* < 1/2$ represent the beginning, middle, and end of acceleration, respectively. The phase for $1/2 < t^*/T^* < 2/3$, $2/3 < t^*/T^* < 5/6$, and $5/6 < t^*/T^* < 1$ represent the beginning, middle, and end of deceleration, respectively.

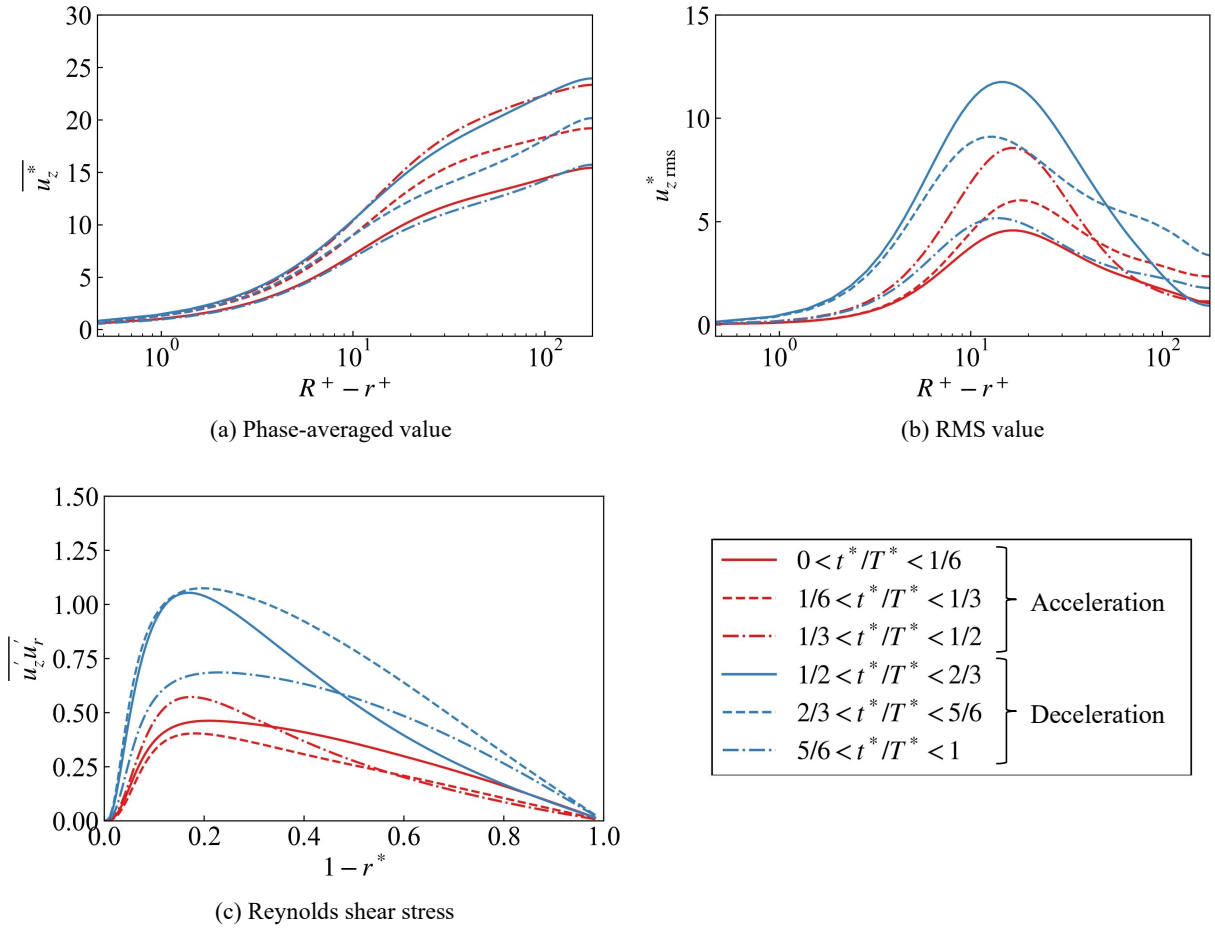

(a) Phase-averaged value

(b) RMS value

(c) Reynolds shear stress

Figure 6. Radial profiles of phase-averaged streamwise velocity, RMS value of phase-averaged streamwise velocity fluctuations, and Reynolds shear stress.

The phase-averaged streamwise velocity has in all phases a minimum value near the wall and a maximum value at the pipe center and increases from near the wall to the pipe center. In the entire region from the wall to the pipe center, the streamwise velocity increases the beginning, middle, and end of acceleration, in that order. On the other hand, that decreases the beginning, middle, and end of deceleration, in that order. In other words, the streamwise velocity increases and decreases with the acceleration and deceleration of the pulsating flow.

In the RMS value, it has a minimum value near the wall, increases from the viscous sub-layer to the buffer layer, and decreases from the buffer layer to the pipe center in all phases. The maximum RMS value increases from the beginning of acceleration to the end, while it decreases from the beginning of deceleration to the end. Therefore, in pulsating flow, turbulence increase with acceleration and decreases with deceleration.

In the Reynold shear stress, the values are zero at the wall and the pipe center, and the values increase rapidly and then decrease slowly from the wall to the pipe center for all phases. The Reynolds shear stress during acceleration is lower than that during deceleration. Comparing Figs. 5 and 6, there is a high correlation between the increase or decrease in the vortex and the increase or decrease in the Reynolds shear stress due to the acceleration and the deceleration. Therefore, in pulsating flow, the vortices increase during the deceleration term, and the turbulent momentum transfer becomes more active.

Generalizability of Time Delay NN-RNN Model

Figure 7 shows the prediction results of phase-averaged streamwise velocity during the acceleration and deceleration terms along with the prediction results by the previous model without TDNN (Yamaguchi et al., 2019). The prediction results of both models reproduce the monotonic increase of the streamwise velocity from zero at the wall to the maximum at the center of the pipe. In the outer layer, the present model with TDNN has higher prediction accuracy than that without TDNN during the acceleration term.

Figure 8 shows the prediction results of the RMS value of phase-averaged streamwise velocity fluctuations during the acceleration term and deceleration term. Focusing on the viscous sub-layer and the buffer layer, the accuracy of both the models is high during the acceleration term, however, the accuracy of the present model with TDNN is higher than that without TDNN during the deceleration term. On the other hand, focusing on the outer layer, the accuracy of both models is low in all phases.

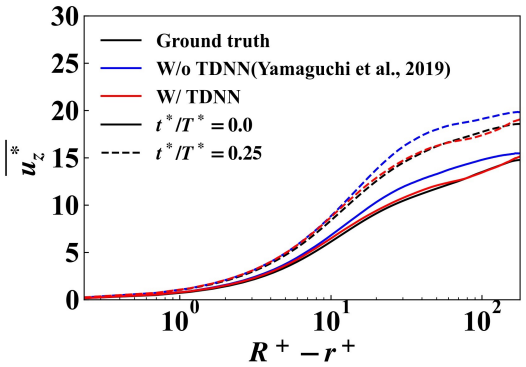

(a) Acceleration

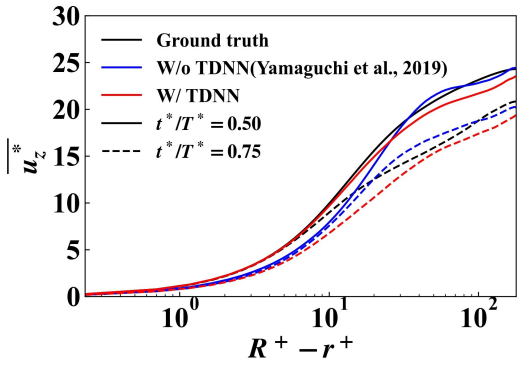

(b) Deceleration

Figure 7. Radial profiles of phase-averaged streamwise velocity.

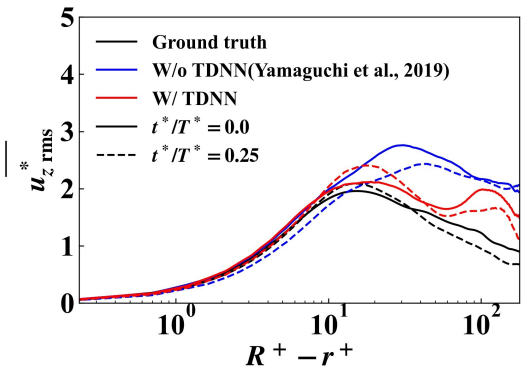

(a) Acceleration

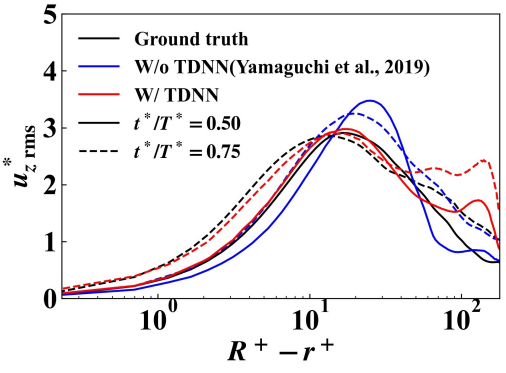

(b) Deceleration

Figure 8. Radial profiles of RMS value of phase-averaged streamwise velocity fluctuations.

Figure 9 shows the prediction and ground truth of phase-averaged bulk velocity u^*_b. The relative error and correlation coefficients are 3.8% and 0.98 without TDNN, −3.4%, and 0.99 with TDNN, respectively. The correlation coefficients of both with TDNN and without TDNN are more than 0.95. The magnitude of the relative errors of both are less than 5 %. Hence, both models can predict the periodic change and the average value for one period with high accuracy. In the bulk velocity, the phase difference between ground truth and prediction with TDNN is smaller than without TDNN. It is because the time change of pulsating waves can be trained by TDNN.

Figure 10 shows the prediction and ground truth of phase-averaged wall shear stress τ^*_w. The relative error and correlation coefficients are −13.0% and 0.41 without TDNN, −6.1%, and 0.75 with TDNN, respectively. The correlation coefficient with TDNN is larger than that without TDNN, and the magnitude of the relative error with TDNN is smaller than without TDNN, which means that the prediction accuracy of the wall shear stress is improved when the TDNN is introduced. In addition, the prediction results of wall shear stress correspond with the ground truth at t^*/T^* =0.0 ~ 0.3 without TDNN, at t^*/T^* =0.0 ~ 0.5 with TDNN. In other words, it can be said that the introduction of TDNN improves prediction accuracy. However, the prediction accuracy is low at t^*/T^* =0.5 ~ 1.0 during deceleration. This is suggested by the lower accuracy of the RMS value near the wall during the deceleration term compared to the acceleration term.

The phase-averaged bulk velocity and wall shear stress for each sinusoidal pulsating wave included in the training data are calculated, and then the averaged values for each of them are calculated. As a result, it is found that these values are consistent with the true values. Therefore, in the current parameter range, the response of the pulsating turbulent pipe flow is high linearity. Nevertheless, the generalizability of the training model is not sufficient because it does not predict statistics with very high accuracy.

Figure 11 shows the prediction and ground truth of phase-averaged skin friction coefficient C_f. The relative error and correlation coefficients are −18.6% and 0.97 without TDNN, −1.0%, and 0.95 with TDNN, respectively. The correlation coefficients of both without TDNN and with TDNN are more than 0.95, which indicates that both models can predict the periodic change of the skin friction coefficient. On the other hand, because the absolute value of the relative error of the model with TDNN is smaller than that without TDNN, the model becomes to accurately predict the average of the skin friction coefficient to introduce TDNN. In other words, compared to the previous study, this study can accurately predict the skin friction coefficient, which determines ultimately the drag reduction effect.

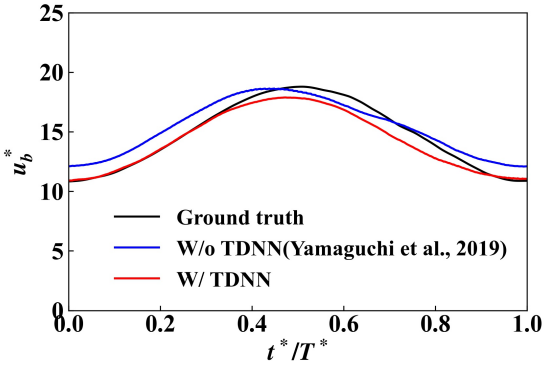

Figure 9. Prediction and ground truth of phase-averaged bulk velocity u^*_b.

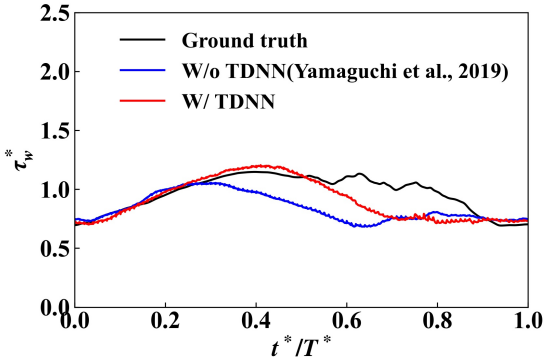

Figure 10. Prediction and ground truth of phase-averaged wall shear stress τ^*_w.

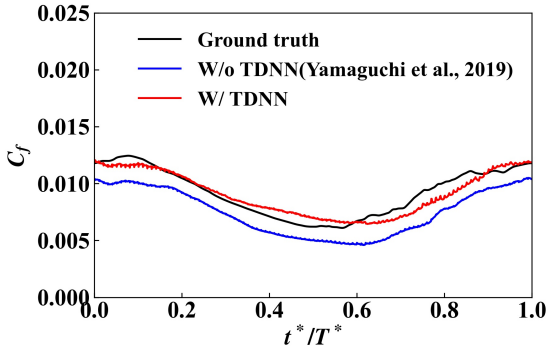

Figure11. Prediction and ground truth of phase-averaged skin friction coefficient C_f.

CONCLUSIONS AND OUTLOOK

The deep learning model predicted the spatiotemporal development of pulsating turbulent pipe flow. To improve the generalizability of the model, the time delay NN-RNN model was constructed by combining TDNN with the previous LSTM encoder-decoder model. The model has predicted flow fields for pulsating flow which are training data (A^*, T^*) = (4, 5), (5, 4), (6, 5), and (5, 6), and test data (A^*, T^*) = (5, 5). The new model can predict streamwise velocity and RMS value of that fluctuations more accurately than the previous model. Therefore, the generalizability of the model is improved. However, despite the high linearity of the pulsating flow response, the prediction of statistics for the bulk velocity and wall share stress is low accuracy. Hence, the generalizability of the training model for this study is not sufficient.

REFERENCES

Manna, M., and Vacca, A., 2008, "Spectral Dynamic of Pulsating Turbulent Pipe Flow", *Computers and Fluids*, Vol. 37, Issue 7, pp.825-835.

Lodahl, C. R., Sumer, B. M., and Fredsøe, J., 1998, "Turbulent Combined Oscillatory Flow and Current in a Pipe", *Journal of Fluid Mechanics*, Vol. 373, pp. 313-348.

Brunton, S. L., Noack, B. R., and Koumoutsakos, P., 2020, "Machine Learning for Fluid Mechanics", *Annual Review of Fluid Mechanics*, Vol. 52, pp. 477-508.

Fan, S., Fei, J., Guo, X. W., Yang, C., and Revell, A., 2021, "CNN+LSTM Accelerated Turbulent Flow Simulation with Link-Wise Artificial Compressibility Method", *Proceedings, 50th International Conference on Parallel Processing*, No. 38, pp. 1-10.

Giannopoulos, A., and Aider, J. L., 2020, "Prediction of the Dynamics of a Backward-Facing Step Flow Using Focused Time-Delay Neural Networks and Particle Image Velocimetry Data-Sets", *International Journal of Heat and Fluid Flow*, Vol. 82, 108533.

Yamaguchi, R., Mitsuishi, A., Shimura, T., Iwamoto, K., and Murata, A., 2019, "Decomposition of Friction Drag and Heat Transfer in Pulsating Turbulent Pipe Flow", *Proceedings, 2nd Pacific Rim Thermal Engineering Conference*, PRTEC-24093.

Fukagata, K., and Kasagi, N., 2002, "Highly Energy-Conservative Finite Difference Method for the Cylindrical Coordinate System", *Journal of Computational Physics*, Vol. 181, Issue 2, pp. 478-498.

Spalart, P. R., Moser, R. D., and Rogers, M. M., 1991, "Spectral Methods for the Navier-Stokes Equations with One Infinite and Two Periodic Directions", *Journal of Computational Physics*, Vol. 96, Issue 2, pp. 297-324.